50th AIAA Aerospace Sciences Meeting including the New Horizons Forum and Aerospace Exposition
09 - 12 January 2012, Nashville, Tennessee

AIAA 2012-1106

Boundary layer transition in high-speed flows due to roughness

Prahladh S. Iyer *, Suman Muppidi †& Krishnan Mahesh ‡
University of Minnesota, Minneapolis, Minnesota, 55455, USA

Direct numerical simulation (DNS) is used to study the effect of individual (hemispherical) and distributed roughness on supersonic flat plate boundary layers. In both cases, roughness generates a shear layer and counter–rotating pairs of unsteady streamwise vortices. The vortices perturb the shear layer, resulting in trains of hairpin vortices and a highly unsteady flow. Mach 3.37 flow past a hemispherical bump is studied by varying the boundary layer thickness (k/δ = 2.54, 1.0, 0.25 & 0.125). Transition occurs in all cases, and the essential mechanism of transition appears to be similar. At smaller boundary layer thickness, multiple trains of hairpin vortices are observed immediately downstream of the roughness, while a single train of hairpin vortices is observed at larger δ. This behavior is explained by the influence of the boundary layer thickness on the separation vortices upstream of the roughness element. Mach 2.9 flow past distributed roughness results in a fully turbulent flow. Mean velocity profiles show spanwise inhomogeneity in the transitional region, with the flow becoming more homogenous downstream. Spanwise spectra initially exhibit only the wavelength of the roughness surface. Then, the energy at smaller wavelengths increases resulting in a broadband spectra downstream. Temporal spectra in the transitional region are characterized by the frequency of the unsteady vortices and a higher frequency corresponding to the shear layer breakdown. The magnitude of wall–pressure fluctuations is observed to be greater in the transitional region than in the turbulent region, where a good agreement with recent experiments is obtained.

I. Introduction

High-speed transition results in increased thermal and aerodynamic loading and influences the design of supersonic/hypersonic vehicles. Transition can be triggered by surface roughness, both discrete and distributed. Roughness in practical surfaces can occur as steps, gaps, screw threads, or ablation effects of thermal protective systems. Review articles by Reda (2002) and Schneider (2008) summarize the work on roughness–induced transition in hypersonic flows. Transition is affected by factors such as the shape and size of roughness, arrangement, and distributed *vs.* individual roughness. It has been observed that distributed roughness causes transition at a lower Reynolds number compared to individual roughness elements (Reda 2002). Empirical models to predict transition do not account for the effects of pressure gradient, surface temperature etc, and are not always reliable (Reshotko 2007). Furthermore, finite sized roughness bypasses the Tollmein–Schlichting route to transition. High fidelity numerical simulations can provide valuable insights into the underlying transition mechanisms.

The objective of this work is to study the effect of distributed and individual roughness elements on transition of laminar flat plate supersonic boundary layers, using direct numerical simulations (DNS). The simulations use a novel algorithm described in Park & Mahesh (2007) to simulate compressible flows in complex geometries. Iyer *et. al.* (2011) described the phenomenology of transition in high speed flat plate boundary layers using simulations of (i) flow past an individual hemispherical roughness element at Mach 3.37, 5.26 and 8.23, and (ii) flow past distributed roughness at Mach 2.9. The simulations of flow past a hemisphere show good qualitative agreement with the experiments by Danehy *et. al.* (2009). At Mach 3.37

*Graduate student, Dept. of Aerospace Engineering and Mechanics, University of Minnesota, MN 55455, Student member.
†Research associate, Aerospace Engineering & Mechanics, AIAA member
‡Professor, Aerospace Engineering & Mechanics, AIAA Associate Fellow

and 5.26, the flow appears unsteady downstream of the roughness element while the flow remains laminar at Mach 8.23. The roughness element causes the incoming boundary layer to separate, generating a system of vortices that wrap around and give rise to coherent streamwise vortices. These vortices are observed to be unsteady, and the interaction between the separated shear layer and the unsteady streamwise vortices causes shear layer breakdown, formation of hairpin vortices, increased heat transfer and skin friction at the wall, and a highly unsteady flow downstream of the roughness element. Muppidi & Mahesh (2012) present a detailed view of the transition due to distributed roughness at Mach 2.9. The mechanism is similar to transition due to individual roughness element – transition appears via the breakdown of a shear layer perturbed by pairs of streamwise vortices. The shear layer is curved and forms since the roughness decelerates the near-wall fluid. Examination of the pressure and velocity fields show that the streamwise vortices are generated due to the surface force (impulse) exerted by the roughness on the near–wall fluid. Mean flow in the turbulent region shows good agreement with available results for turbulent boundary layers indicating that roughness results in a fully turbulent flow.

This paper is a continuation of the work presented in Iyer *et. al.* (2011). For the single (hemispherical) roughness element, we present the effect of boundary layer thickness on the transition process at Mach number 3.37, to verify the validity of the phenomenology proposed in Iyer *et. al.* for small roughness sizes. For distributed roughness, the paper presents the spanwise inhomogeneity of the mean flow in the transitional region, and the spanwise and temporal spectra, and relates them to the transition mechanism proposed in Iyer *et. al.* and Muppidi & Mahesh (2012). The paper also presents data for pressure fluctuations along the wall. Fluctuations in the turbulent region agree with available results, and are lower than the wall pressure r.m.s. in the transitional part of the domain. The paper is organized as follows. Section II provides an overview of the numerical scheme. Section III presents the results for flow past the hemisphere including the problem description and simulation parameters. Section IV presents results for the flow past distributed roughness.

II. Algorithm

The simulations use an algorithm developed by Park & Mahesh (2007) for solving the compressible Navier–Stokes equations on unstructured grids:

$$\begin{aligned} \frac{\partial \rho}{\partial t} &= -\frac{\partial}{\partial x_k}\left(\rho u_k\right), \\ \frac{\partial \rho u_i}{\partial t} &= -\frac{\partial}{\partial x_k}\left(\rho u_i u_k + p\delta_{ik} - \sigma_{ik}\right), \text{ and} \\ \frac{\partial E_T}{\partial t} &= -\frac{\partial}{\partial x_k}\left\{\left(E_T + p\right) u_k - \sigma_{ik} u_i - Q_k\right\}, \end{aligned} \tag{1}$$

where ρ, u_i, p and E_T are density, velocity, pressure and total energy, respectively. The viscous stress σ_{ij} and heat flux Q_i are given by

$$\sigma_{ij} = \frac{\mu}{Re}\left(\frac{\partial u_i}{\partial x_j} + \frac{\partial u_j}{\partial x_i} - \frac{2}{3}\frac{\partial u_k}{\partial x_k}\delta_{ij}\right), \tag{2}$$

$$Q_i = \frac{\mu}{(\gamma-1)M_\infty^2 RePr}\frac{\partial T}{\partial x_i} \tag{3}$$

after non-dimensionalization, where Re, M_∞ and Pr denote the Reynolds number, Mach number and Prandtl number respectively. Discretization of the governing equations is performed using a cell–centered finite volume formulation, and the algorithm uses a shock–capturing scheme applied in a predictor–corrector manner. The predictor step is non–dissipative, ensuring that numerical dissipation is localized to the immediate vicinity of discontinuities. Details of the algorithm are provided in Park & Mahesh (2007).

III. Flow past individual hemispherical roughness

A. Problem description

A laminar boundary layer at M_∞=3.37 and $Re_k = u_e k/\nu_e$=4560 is incident on a hemispherical bump, a schematic of which is shown in figure 1. The domain extends from -25 to 25 in the streamwise direction (x),

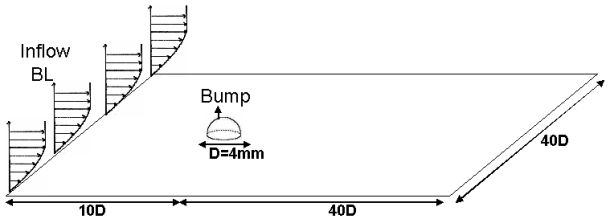

Figure 1. Schematic of the flow past an isolated hemispherical roughness element.

-20 to 20 in the spanwise direction (z) and -10 to 10 in the wall normal direction (y). All lengths are non-dimensionalized with respect to the diameter of the bump, D. The bump is located at x=-15. A compressible similarity solution is prescribed at the inflow. Zero gradient conditions are used at the outflow, top wall and side walls. A non–reflecting boundary condition is used on all boundaries (excluding the flat plate) to remove any acoustic reflections. The flat plate is maintained at an isothermal condition with $T_{wall} = 300K$ ($T_\infty = 340.48K$). The computational mesh is unstructured and consists of 16 million elements.

The focus of the present work is to study the effect of boundary layer thickness on the transition mechanism. Four values of k/δ (table 1) are considered, where k is the roughness height and δ is the boundary layer thickness of the laminar boundary layer at the location of the roughness if it were absent. Inflow boundary layer conditions are prescribed from the compressible similarity solution such that the corresponding k/δ is obtained at the location of the roughness. The corresponding Re_x and Re_θ for the laminar boundary layer at the location of the roughness are specified in table 1 where x is the distance from the leading edge of the flat plate.

k/δ	Re_x	Re_θ
2.54	91207.7	193.08
1.0	5.472×10^5	473.94
0.25	8.738×10^6	1894.38
0.125	34.883×10^6	3786.03

Table 1. Parameters for flow past discrete hemispherical bump.

B. Summary of past work

Flow past a cylindrical roughness element on a flat plate at Mach 8.12 and the flow past a hemispherical bump at Mach 3.37, 5.26 and 8.23 were studied in Iyer *et. al.* (2011). Velocity profiles for the Mach 8.12 case were compared to the experiments of Bathel *et. al.* (2010) in the symmetry and wall parallel planes and good agreement was observed. For the flow past a hemispherical bump, it was observed that Mach 3.37 and 5.26 flows transitioned downstream whereas Mach 8.23 flow remained laminar. The essential mechanism of transition is briefly discussed here. As the boundary layer approaches the roughness element, fluid decelerates, and three dimensional separation is observed, giving rise to a system of vortices upstream of the roughness. These vortices wrap around the hemisphere, giving rise to counter-rotating streamwise vortices downstream of the roughness. For the cases that transitioned, these vortices were unsteady and perturbed the shear layer above it which resulted in the shedding of coherent hairpin-shaped vortices. These vortices form a more complex system of vortices as they move downstream, giving rise to an increasingly broadband flow far downstream of the roughness. A rise in the skin friction coefficient was observed downstream of the bump for the cases that transitioned while for Mach 8.23, there was a rise immediately downstream which then approached the laminar value with increasing downstream distance. Figure 2 shows the instantaneous density gradient contours for the Mach 3.37 case from Iyer *et. al.* (2011). The spanwise symmetry plane, wall parallel plane $0.05D$ from the flat plate and a streamwise plane $10D$ downstream of the roughness is shown in the figure. The flow conditions for this case is the same as the cases studied in the current paper with the exception of Re_k which is twice the current value. Shocks produced due to the roughness element

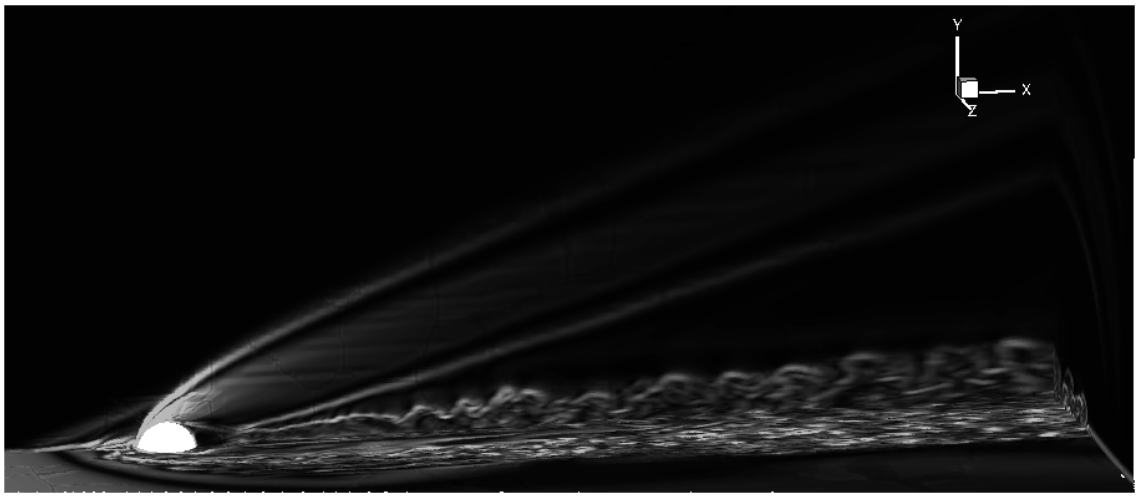

Figure 2. Instantaneous density gradient contours corresponding to Mach 3.37 case from Iyer *et. al.* (2011).

are clearly visible. Downstream of the roughness, the break-up of the shear layer in the symmetry plane is visible. Further downstream the flow appears highly unsteady in both the symmetry and wall-parallel planes. In the wall-parallel plane, the unsteady features spread in the spanwise direction with increasing downstream distance.

C. Effect of varying boundary layer thickness

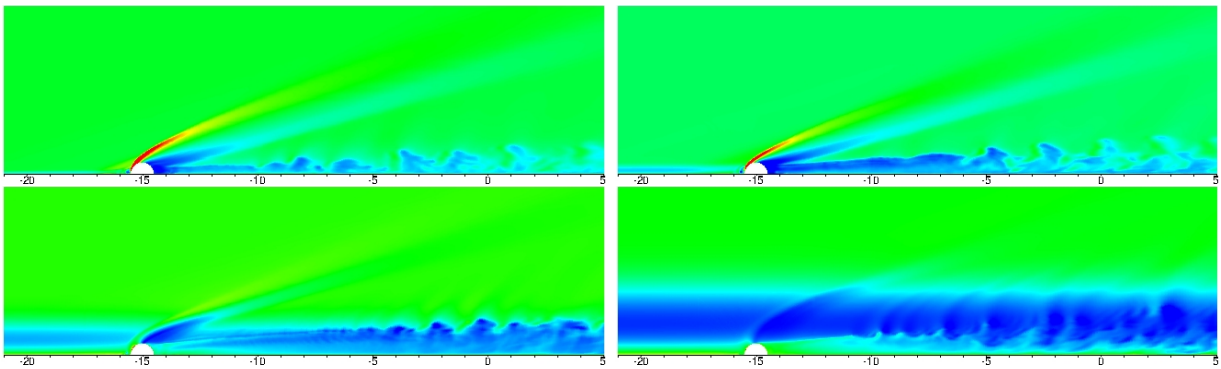

Figure 3. Instantaneous density contours in the z =0 symmetry plane for k/δ = 2.54 (top-left), 1.0 (top-right), 0.25 (bottom-left) and 0.125 (bottom-right).

In this paper, we study the effect of varying the boundary layer thickness relative to the roughness height. While the essential features of transition are similar for the four cases studied, some differences are observed. Instantaneous density contours for the four cases in the symmetry plane are shown in figure 3. Note that all four cases appear transitional downstream of the roughness. Upstream of the bump, the difference in boundary layer thickness is clearly seen in the figure for the four cases. The shock produced due to the roughness is visible for all cases with $k/\delta = 2.54$ having the strongest shock due to higher local Mach number at the height of the roughness.

The laminar boundary layer separates upstream of the bump giving rise to a system of spanwise vortices as shown in figure 4. Instantaneous streamlines are plotted in the symmetry plane. It can be seen that with decreasing k/δ, the separation length decreases. This can be understood by a simple scaling argument. Consider a point close to the flat plate upstream of the bump. Since the wall condition is same for all four cases, the density at the chosen point would also roughly be the same. Its momentum would scale with the

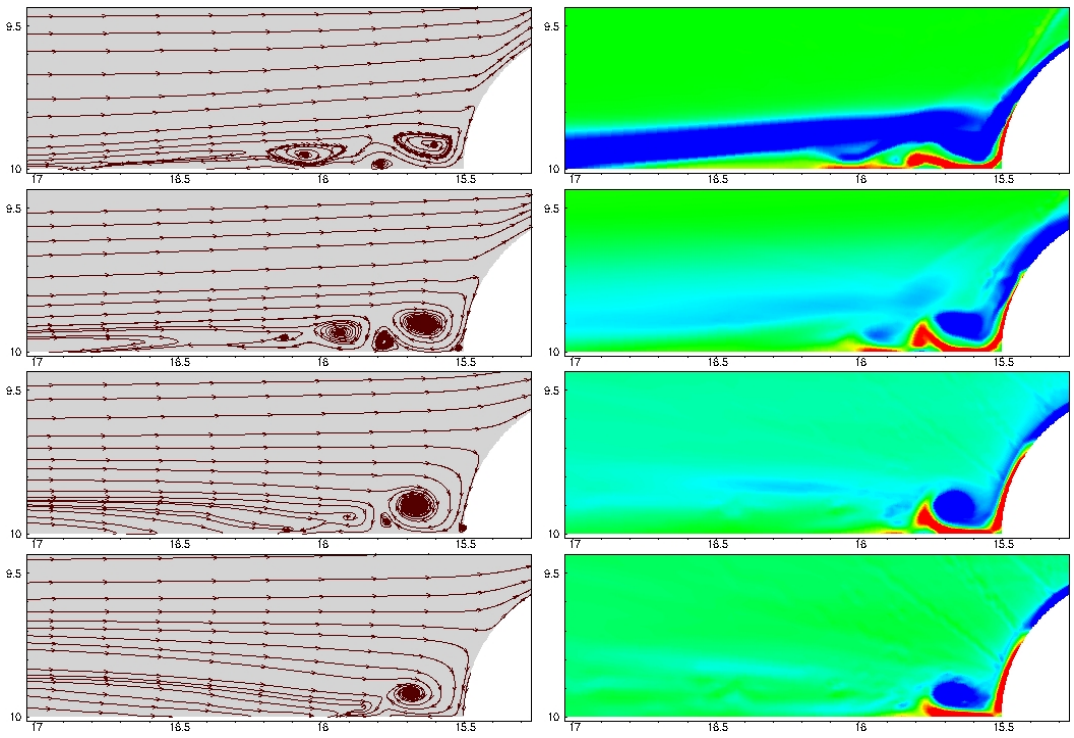

Figure 4. Instantaneous streamlines (left) and ω_z contours (right) in the z =0 symmetry plane upstream of the bump for k/δ =2.54,1.0,0.25 and 0.125 (top to bottom).

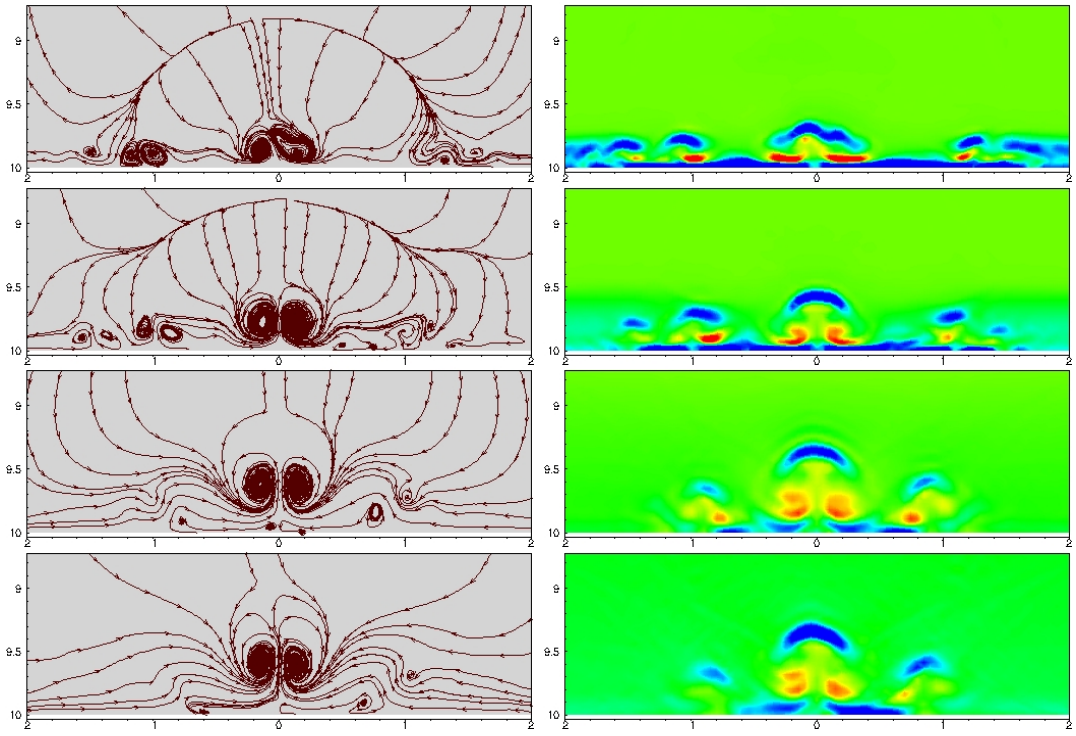

Figure 5. Instantaneous streamlines (left) and ω_x contours (right) at x =2D downstream of the bump for k/δ =2.54,1.0,0.25 and 0.125 (top to bottom).

local u velocity while the pressure difference would roughly scale with $u\partial u/\partial x$. Since the local u is lower for a larger δ, the pressure difference relative to the momentum is going to be lower for the larger δ case thereby allowing the flow to separate later. From the figure, note that the number of vortices upstream is different for the four cases with the larger k/δ cases having more vortices. This is in qualitative agreement with the result of Baker (1979), who studied the flow past a cylindrical protuberance at incompressible speeds and found that at a fixed Re_k, a higher k/δ gives rise to more separation vortices upstream. From the figure, we see that the length scale of the primary vortex(largest vortex) is roughly the same for all four cases i.e. the approximate location on the bump at which streamlines separate is roughly the same. Thus, it appears that the length scale of the upstream vortices is more a function of the shape of the roughness element. Also shown in figure 4 are the instantaneous ω_z contours to indicate the strength of the vortices. Note that the color scheme used is different for all cases and that the strength of the vortices decreases with decreasing k/δ. Relative to the primary vortex, it can be seen that the secondary vortex (x=-16) becomes weaker with decreasing k/δ. As will be seen later, this has a bearing on the transitional nature of the flow downstream.

The spanwise vortices wrap around the bump producing a system of counter-rotating streamwise vortices downstream of the bump. Figure 5 shows instantaneous streamlines and ω_x contours at a plane $2D$ downstream of the center of the bump. Counter-rotating streamwise vortices are formed close to the symmetry plane and away from the symmetry plane on either side. Depending on their strength and sense of rotation, the streamwise vortices move closer or away from the symmetry plane due to the induced velocity from the mirror vortices below the flat plate. The counter-rotating vortices can have a net upwash or downwash depending on their sense of rotation. From figure 5, it can be seen that the counter-rotating vortex pair at both at and away from the symmetry plane have a net upwash i.e. they perturb the shear layer above them. The center of the symmetry plane vortices moves away from the flat plate with decreasing k/δ. This could be due to the fact that the induced velocity by the counter rotating vortex relative to the streamwise velocity at that downstream location is higher for the lower k/δ cases.

The streamwise vortices perturb the shear layer above it as seen in figure 5 resulting in the shedding of hairpin-shaped vortices. Iso-contours of the Q criterion in figure 6 shows the hairpin-shaped vortices produced downstream of the roughness. Closer to the bump, the location of the hairpin vortices correspond to the location of counter-rotating streamwise vortices. Farther downstream, the trains of hairpin vortices give rise to secondary vortices resulting in the spanwise spreading of the vortices. Note that for k/δ=2.54 and 1.0, three trains of hairpin vortices are observed closer to the roughness while for smaller k/δ cases, a single train of hairpin vortices is observed. This can be attributed to the fact that the secondary spanwise vortex upstream of the bump was weak for the smaller k/δ cases, resulting in weak counter-rotating streamwise vortices away from the symmetry plane thereby not perturbing the shear layer enough to shed hairpin vortices. These hairpin vortices cause an increase in the wall skin friction and heat transfer by transporting higher momentum fluid towards the wall and lower momentum fluid away from the wall. For $k/\delta = 0.25, 0.125$, it can be seen that the height of the hairpin vortex is initially of the order of the roughness height, but with increasing distance downstream, it becomes larger and appears to scale with the boundary layer thickness. The rising of the hairpin head with downstream distance could be due to the fact that the central portion of the hairpin has vorticity which induces a net upward velocity similar to the streamwise cut seen in figure 5. The hairpin vortices appear more coherent closer to the bump and become less coherent with increasing downstream distance especially for the larger k/δ cases. It should be noted that in the grid used in the current problem, the streamwise resolution is lower far away from the bump and this could cause the lack of coherence far downstream. On the other hand, as secondary vortices are formed, due to the complex interaction of these vortices, the loss of coherence could also be physical. This will be verified in the future by a higher resolution calculation to assess the effect of resolution on the vortices.

Figure 7 shows the variation of the mean C_f with x for the four cases where $C_f = \mu\partial u/\partial y|_w/(\rho_e u_e^2)$. For k/δ=2.54, C_f vs x is plotted at $0.5D$ away from the symmetry plane while for the other cases, the variation in the symmetry plane is shown. It should be noted that due to the transitional nature of the flow, spanwise inhomogeneity in the mean exists and therefore representative spanwise locations are chosen to show the increase in C_f downstream of the roughness. The laminar C_f is plotted from the compressible similarity solution. Note that the laminar C_f curve flattens out with increasing Re_x in the length of the domain considered. Upstream of the bump, the C_f curve agrees with with the laminar C_f. Just upstream of the bump, C_f becomes negative due to separation for all four cases while downstream, the C_f increases confirming the transitional nature of the flow.

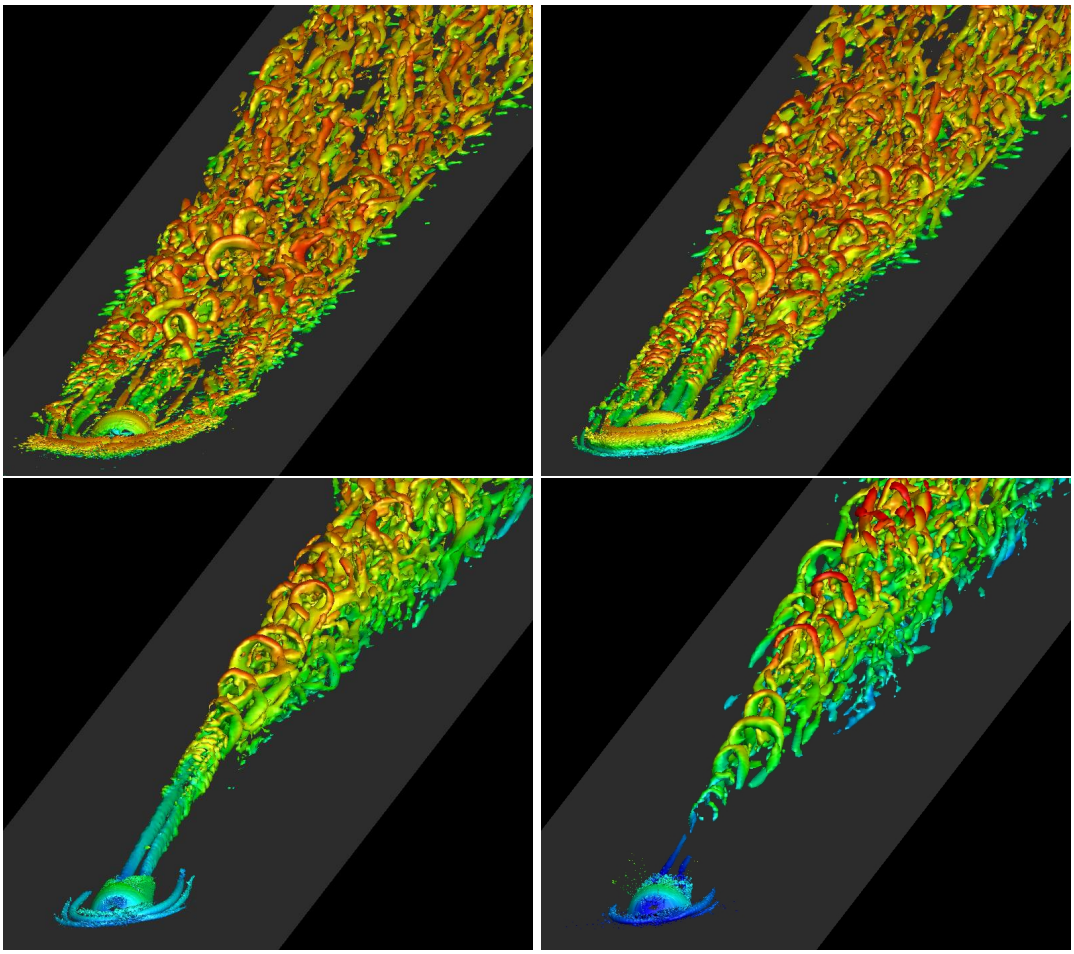

Figure 6. Iso-contour of Q criterion plots colored by streamwise velocity showing hairpin vortices for $k/\delta =$ 2.54 (top-left), 1.0 (top-right), 0.25 (bottom-left) and 0.125 (bottom-right). The hairpin vortices are clearly seen in all cases. With decreasing k/δ, only a single train of hairpin vortices are observed behind the roughness element.

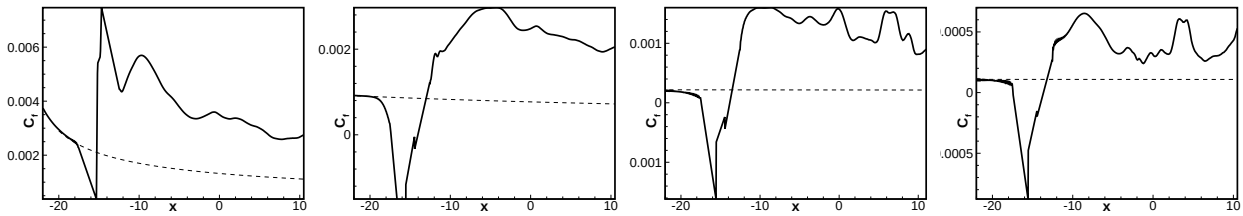

Figure 7. Variation of skin friction coefficient (C_f) with distance x for k/δ =2.54,1.0,0.25 and 0.125 (left to right). Also shown is the C_f from compressible similarity solution (dotted line). Transition occurs at all k/δ values, as seen by the increase in C_f downstream of the roughness.

IV. Flow past distributed roughness

A. Problem description

Figure 8 shows the computational domain and a schematic of the problem. The streamwise and wall–normal directions are x and y, and the domain is periodic in the spanwise z direction. The domain extends 5 inches ($4 < x < 9$) in the streamwise direction, and 0.5 and 0.175 inches in the wall–normal and spanwise directions

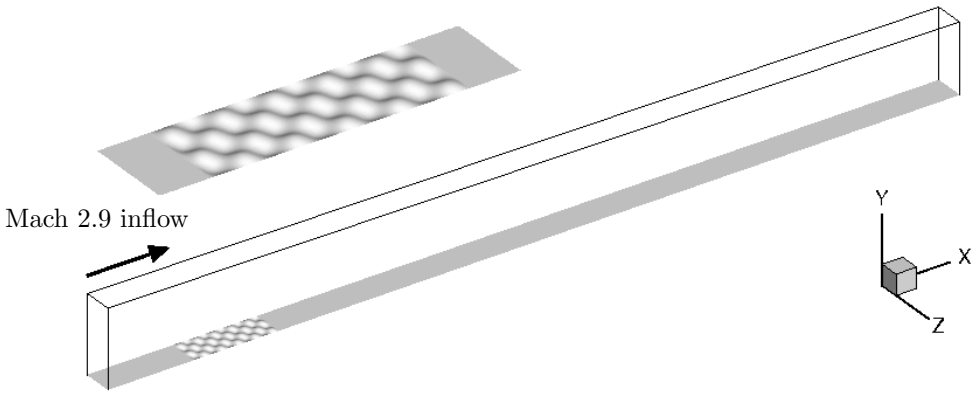

Figure 8. Schematic of the problem shows the extent of the roughness strip along with the coordinate axes. The domain extends from $x = 4.0$ to $x = 9.0$ inches, 0.5 inches in the wall normal direction, and 0.175 inches in the spanwise direction.

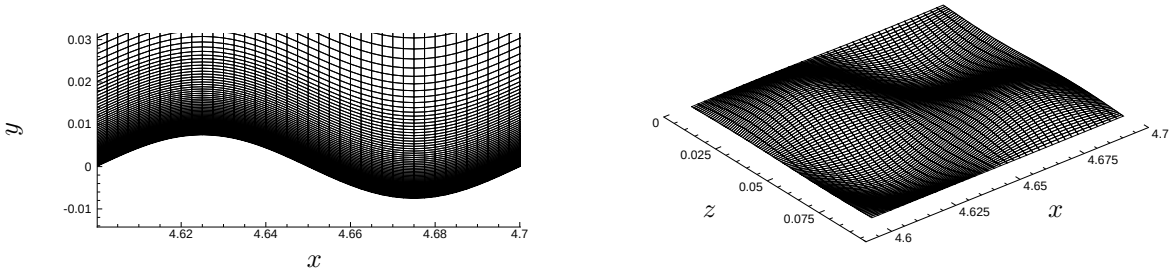

Figure 9. Computational mesh in the roughness region shown on side plane ($x-y$ plane) and along the surface. The figure shows the mesh over one wavelength of the roughness surface.

respectively. A portion of the wall ($4.5 < x < 5.0$) is modeled as a rough surface, as

$$y_{wall} = k\ sin(2\ \pi\ x/\lambda_x)\ sin(2\ \pi\ z/\lambda_z),$$

and the wavelengths λ_x, λ_z are chosen such that the roughness region spans five full wavelengths in the streamwise direction and two in the spanwise direction. k is the peak roughness height, set to be 0.0075 inches ($k/\delta_{inflow} \sim 0.35$). The incoming flow is laminar at Mach 2.9, and with a freestream unit Reynolds number ($Re_\infty = \rho_\infty u_\infty/\nu_\infty$) of 635000 per inch. Isothermal boundary conditions ($T_{wall}/T_\infty = [1+\frac{\gamma-1}{2}M_\infty^2]$) are prescribed at the wall. The computational mesh used for the simulation consists of 36 million hexahedral elements, uniform in x and z, such that $\Delta x = 2.5 \times 10^{-3}$, $\Delta z = 9.1 \times 10^{-4}$ and $\Delta y_{min} = 5 \times 10^{-5}$ (in inches). Figure 9 shows the details of the computational mesh over the roughness element, on $x-y$ and $x-z$ planes, over one wavelength of the surface. Further computational details including boundary conditions are provided in Muppidi & Mahesh (2012).

B. Summary of past work

Results of the DNS (Iyer *et. al.* 2011, Muppidi & Mahesh 2012) show that the incoming laminar boundary layer is modified by the roughness region to generate a shear layer situated over the roughness elements, susceptible to breakdown. The velocity field at the end of the roughness region shows that the mixing layer is not planar, but curved. Roughness also generates pairs of streamwise vortices located underneath the shear layer, and formed as a result of the impulse on the near–wall fluid exerted by the rough surface. Along the streamwise distance, the vortices are observed to become stronger and longer, and become unsteady, advecting in the streamwise direction. Downstream of the roughness region, the interaction of the vortices with the shear layer causes the shear layer to breakdown and induce transition.

This phenomenology is schematically illustrated in figure 10. The roughness region, shown, extends between $x = 4.5$ and 5.0 inches. At $x = 5.0$, the flow is characterized by curved mixing layer and pairs of counter–rotating unsteady vortices underneath. The vortices are shed very periodically, and are fairly

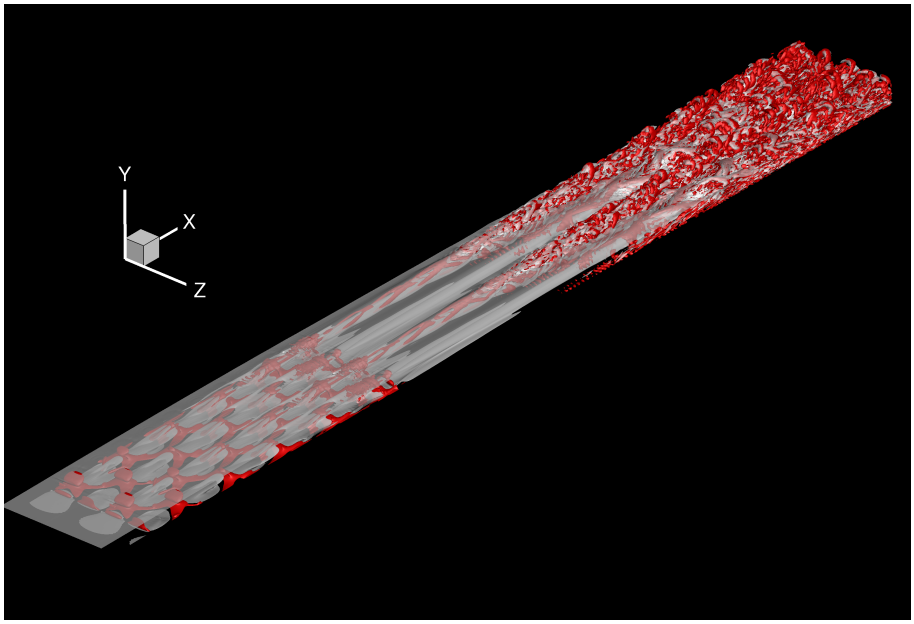

Figure 10. Interaction of the roughness–generated vortices with the shear layer visualized with isosurfaces of vorticity (ω_z =-10) and Q criteria (Q = 40). The vortices are fairly coherent until they reach the shear layer, and this interaction is followed by a turbulent flow downstream.

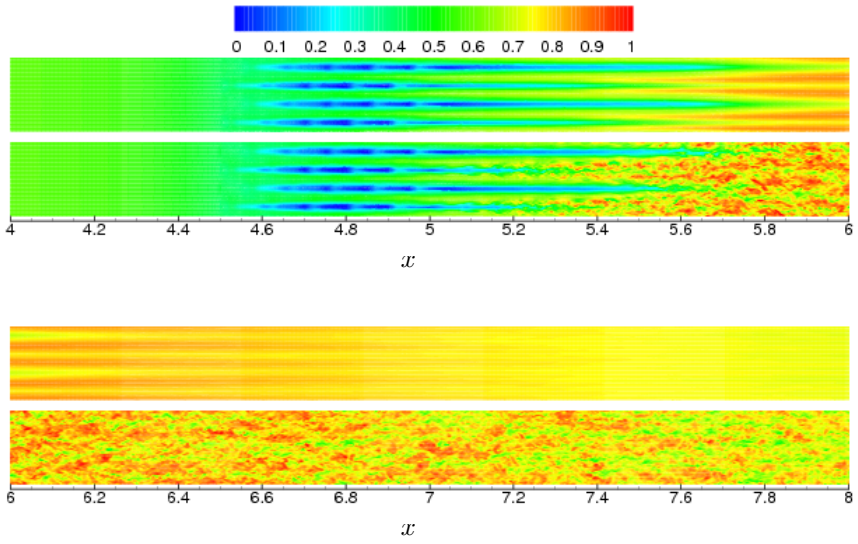

Figure 11. Contours of mean and instantaneous streamwise velocity (u/u_∞) on the plane $y = 0.01$. Note that the computational domain extends from $x = 4.0$ to $x = 9.0$, roughness extends from $x = 4.5$ to $x = 5.0$.

coherent as they advect downstream. They interact with the shear layer, and perturb it at around $x = 5.5$. Past about $x = 6.0$, the flow appears to be visibly turbulent. Detailed comparison of the mean flow in the turbulent region with available data for turbulent boundary layers shows a good agreement, indicating that distributed roughness results in a fully developed boundary layer. This paper analyses the DNS results to examine spanwise homogeneity of the flow in the transitional and turbulent regions, spanwise and temporal spectra of the fluctuations, and the variation of the wall-pressure fluctuations.

C. Spanwise non–uniformity

Figure 11 shows contours of time averaged and instantaneous streamwise velocity (u/u_∞) on a plane parallel to the wall ($y = 0.01$; $y/k \sim 1.34$). The roughness region extends between $x = 4.5$ and 5.0. The figures show that the fluid decelerates as it approaches the roughness region, and regions of higher streamwise velocity exist in between the roughness elements, resulting in alternating streaks of high and low velocity. Immediately downstream of the roughness, transition appears to begin in the line of the crests of the roughness elements, and extend/spread in the spanwise direction. This behavior makes the specification of a single streamwise transition location questionable.

Figure 12 shows the variations of Van Driest transformed velocity across the boundary layer (plotted as a function of y^+) at streamwise locations $x = 5.5$, 6.0, 6.5 and 7.0. The curves in red correspond to various spanwise locations (separated by $\lambda_z/4$) and the black curve is the spanwise–averaged velocity profile. In the transitional region, the velocity profiles show a significant scatter, indicative of spanwise inhomogeneity. At $x = 5.5$, not only is this scatter/deviation the maximum, but the profiles also betray the transitional nature of the flow. With increasing streamwise distance, the differences decrease and practically collapse by $x = 7.0$ indicating a fully turbulent, spanwise–uniform, boundary layer. This inhomogeneity in the transitional region is also observed in the wall quantities, as shown using the skin friction coefficient in figure 13. Between $x = 5.5$ and 6.0, the spanwise–averaged C_f rises steadily while the growth in C_f is locally more rapid/sudden. The contour plot appears relatively uniform past $x = 6.0$.

D. Spanwise spectra

Figure 14 shows the spanwise variations of u (at the y location and time instant corresponding to figure 11) at various streamwise locations. At $x = 4.5$, the velocity profile is characterized by a small deviation from the inflow (uniform) velocity, and a wavelength that equals λ_z (note that spanwise domain $L_z = 2\lambda_z$). However, due to the staggered arrangement of the roughness surface, downstream profiles of velocity show four peaks. Between $x = 5.0$ and 5.5, the profiles exhibit an increase in the high frequency content as the shear layer breaks down.

Figure 15 plots the spanwise spectra of the profiles shown in figure 14. The following observations are made: (*i*) At $x = 4.5$, the only dominant frequency corresponds to λ_z. (*ii*) Immediately downstream, the most dominant wavelength is $0.5\lambda_z$. (*iii*) Between $x = 5.0$ and 5.5, the dominant wavelength is still $0.5\lambda_z$, but there is an increase in the energy content corresponding to λ_z (note that this is the region characterized by the unsteady streamwise vortices and they are separated by λ_z). (*iv*) With increasing streamwise distance, energy at higher wavenumbers increases, and between $x = 6$ and 6.5, the spectra essentially collapse, displaying the behavior characteristic of turbulent boundary layer flows. Note that the turbulent spectra exhibit four orders of decay indicating reasonable spanwise resolution (Moin & Mahesh 1998).

E. Temporal spectra

Figure 16 shows the time history of streamwise velocity at a few x locations along the plane $y = 0.01$ and $z = 0.0$. The time history is dominated by a very periodic variation in u corresponding to the shedding frequency of the streamwise vortex pairs. The roll-up of the shear layer (figure 16 in Muppidi & Mahesh 2012) results in an increased amplitude of the unsteadiness. Downstream locations exhibit higher frequencies as a result of the shear layer break down. Figure 17 shows the temporal spectra of u as a function of x. The spectra appear broadband starting at about $x = 5.5$. Between x=6.0 and 8.0, the spectra show a very close collapse. The following observations are made from figure 17: (*i*) At $x = 5.0$, the the most dominant frequency is 8/unit time indicative of the roughness generated streamwise vortices. The higher frequency content at this location has small amplitude. (*ii*) With increasing x, unsteadiness and hence amplitude across all frequencies increases (in comparison to the amplitude corresponding to 8/unit time). (*iii*) The

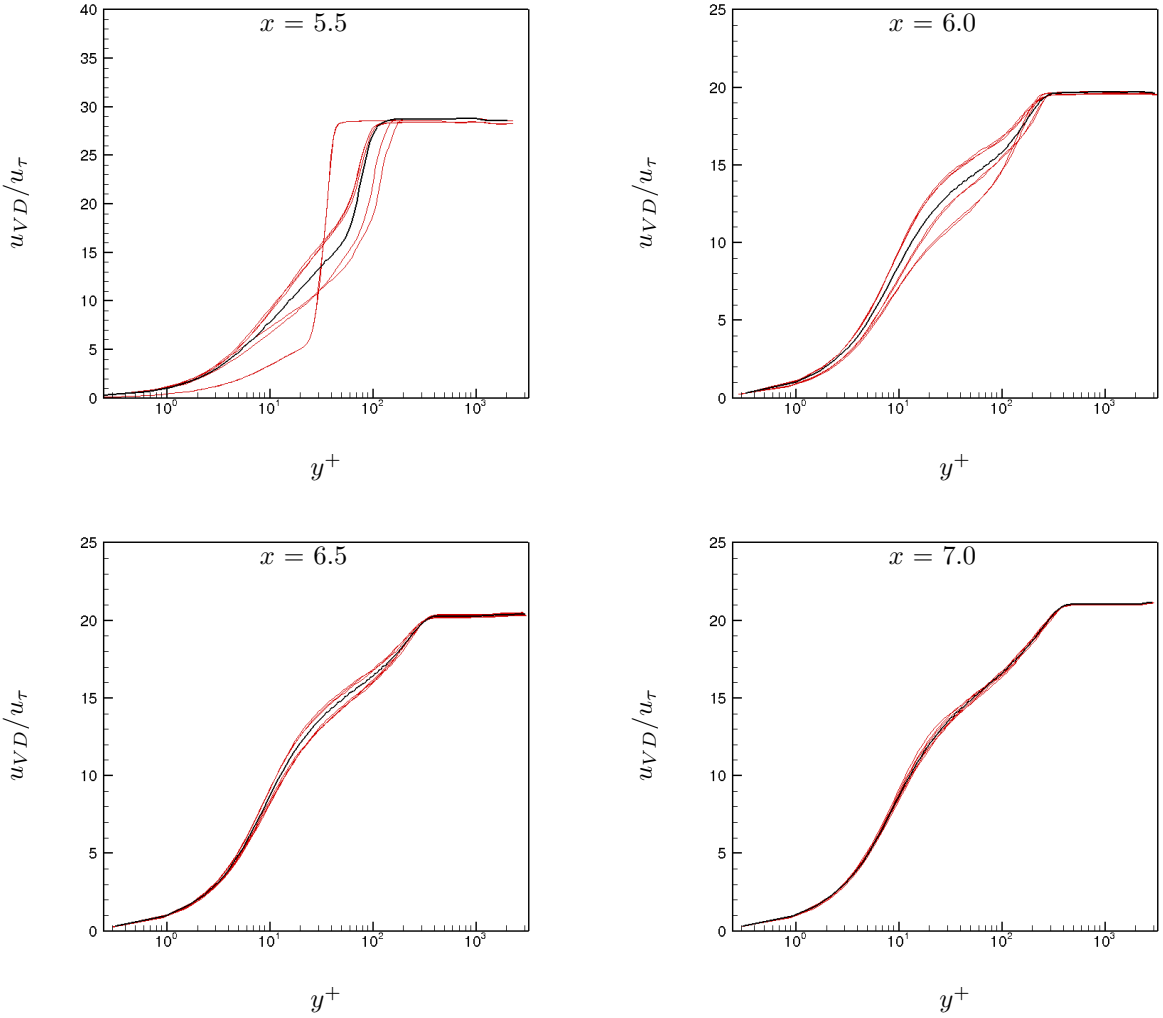

Figure 12. Variation of Van Driest transformed velocity profiles at different spanwise locations (red line) along with the spanwise-averaged profile (black).

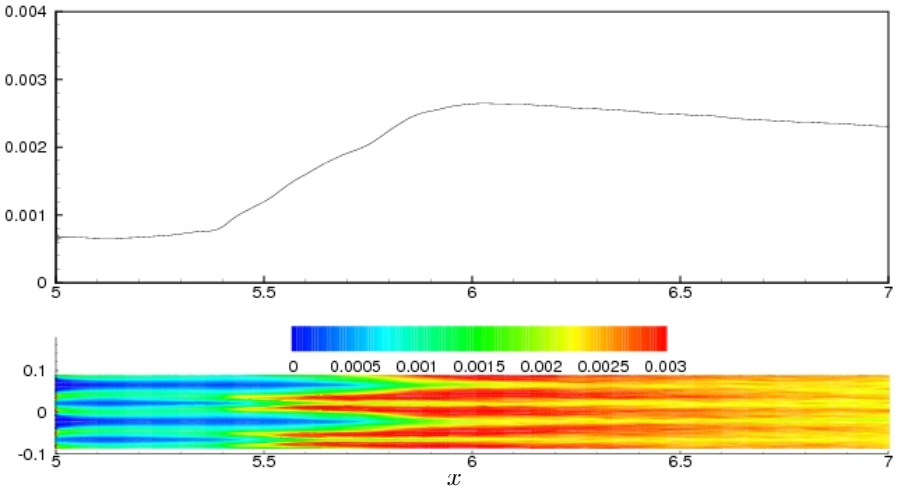

Figure 13. Streamwise variation of skin friction coefficient. Top curve shows span–averaged C_f.

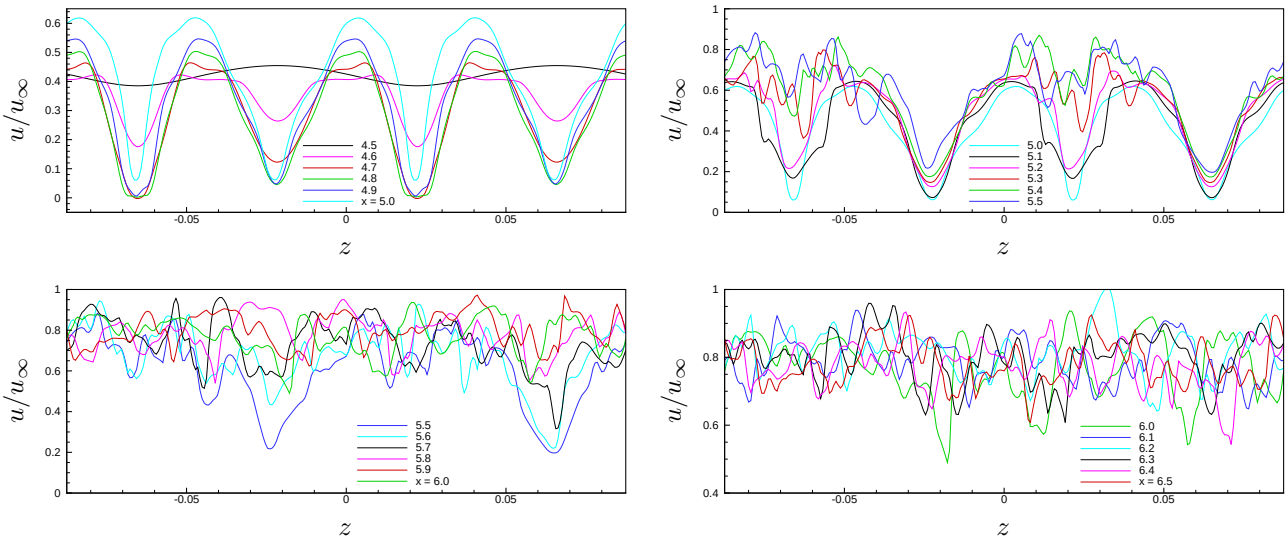

Figure 14. Spanwise profiles of instantaneous velocity (u/u_∞) at $y = 0.01$, plotted at various streamwise locations.

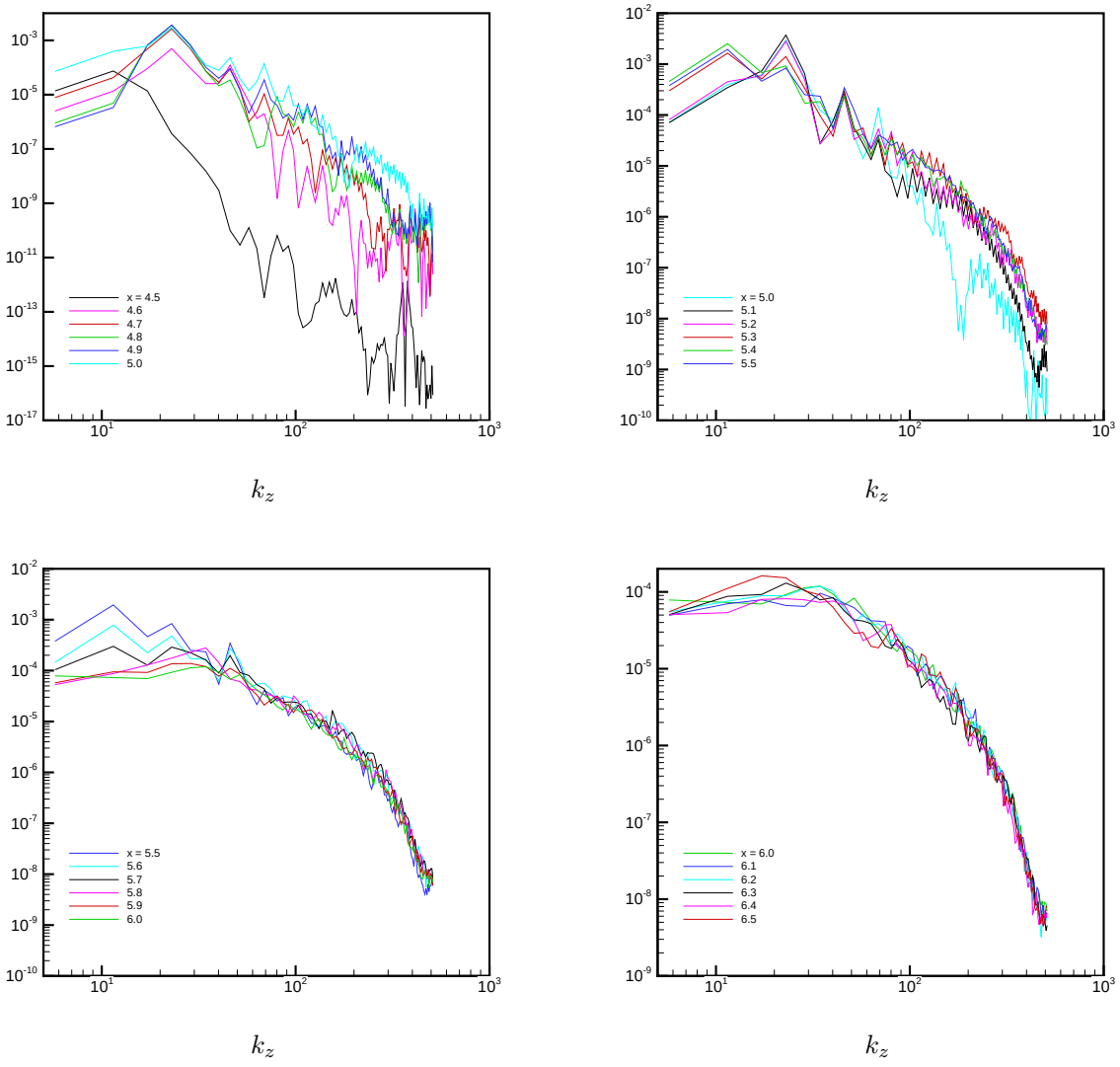

Figure 15. Spanwise (wavenumber) spectra of streamwise velocity (u/u_∞) at $y = 0.01$, plotted at various x locations.

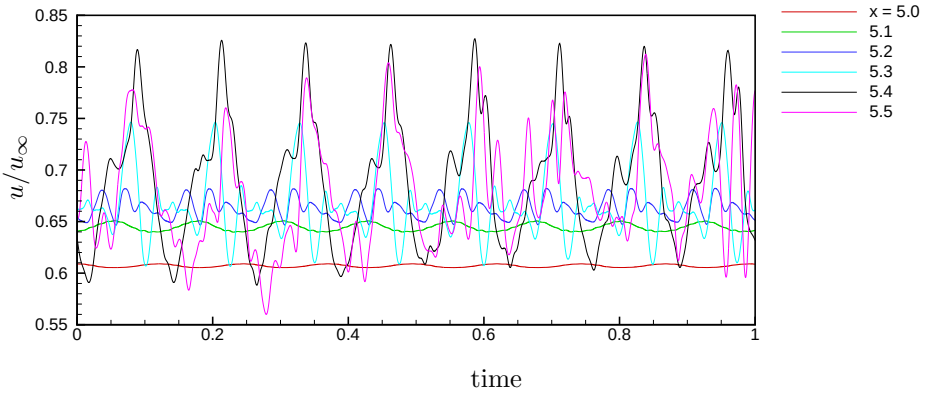

Figure 16. Time history of streamwise velocity in the vicinity of the roughness region, $y = 0.01$.

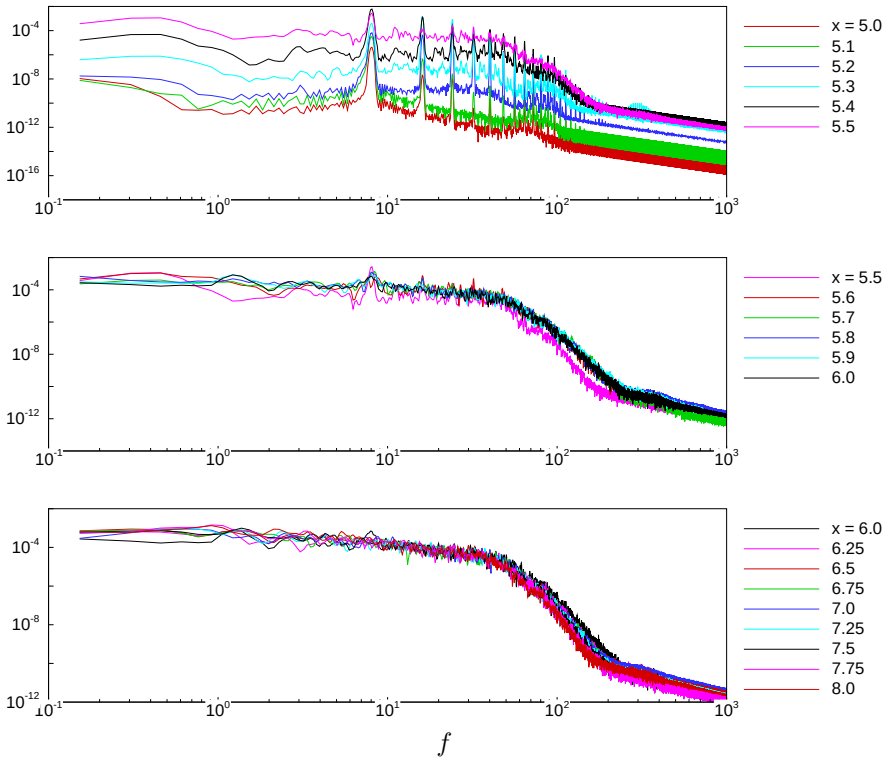

Figure 17. Temporal spectra of streamwise velocity (u/u_∞) at $y = 0.01$, plotted at various x locations.

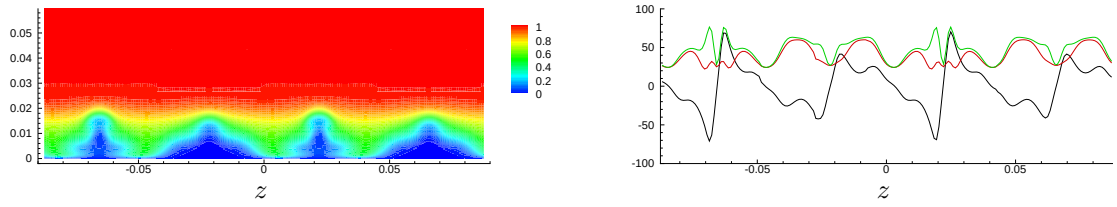

Figure 18. Contours of time–averaged velocity u on the plane $x = 5.0$ show the effect of the roughness region on the incoming velocity field. Velocity field is characterized by sharp gradients. Figure also shows the spanwise variation of $\partial u/\partial z$ (———), $\partial u/\partial y$ (———), and $\sqrt{u_z^2 + u_y^2}$ (———) at $y = 0.01$.

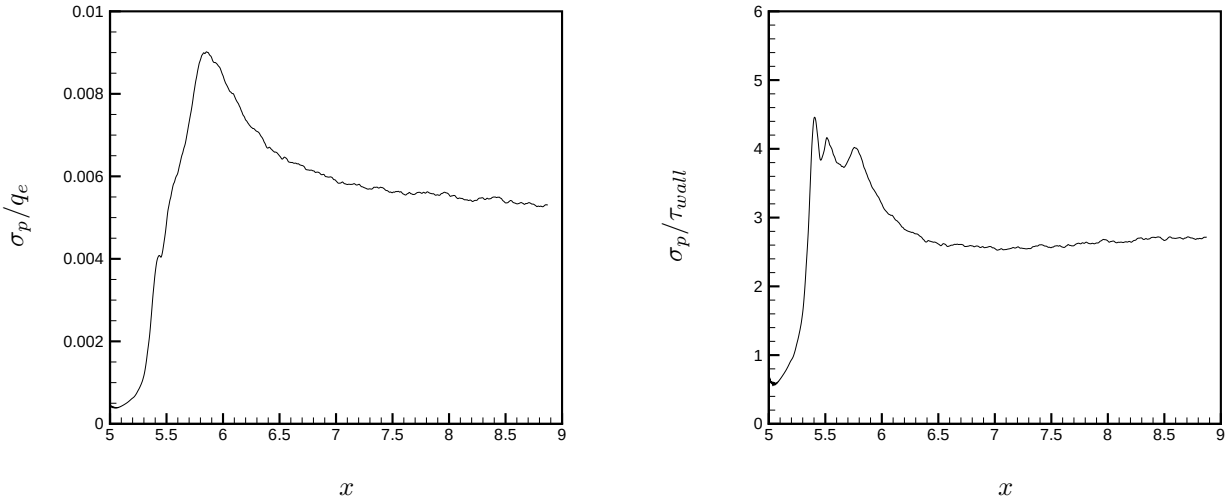

Figure 19. Variation of wall pressure fluctuations (σ_p) with streamwise distance.

evolution toward broadband spectra appears to include unsteadiness in the 70–100/unit time range. This spectral content is visible until about $x = 5.5$.

Ergin & White (2006) present temporal spectra behind a row of roughness elements at low speeds. Their spectra show appreciable energy content around 700 Hz, downstream of the roughness elements. This local peak spreads and disappears as the spectra become more broadband downstream, and the magnitude (700 Hz) is shown to be in agreement with their computation of a representative frequency for the unstable shear layer. Figure 18 presents the spanwise variation of the mean shear $(\partial u/\partial y, \partial u/\partial z)$ at $x = 5.0$ and $y = 0.01$ from the present simulations. Note that the magnitude of the peak gradients corresponds to the frequencies observed in figure 17, strengthening the argument that transition is a result of the shear layer breakdown.

F. Pressure fluctuations

High speed vehicles in transitional/turbulent flow can be subject to high levels of fluctuating pressures, causing vibration and resulting in structural fatigue. It is important to predict the location and magnitude of these pressure fluctuations for the design of reentry vehicles. These predictions are made more difficult if the flow transitions over the surface of the vehicle. Existing correlations for transitional and turbulent pressure fluctuations show significant scatter and provide little physical understanding of the origin of these fluctuations (Casper *et. al.* 2009). Even in fully turbulent boundary layers, the database of pressure fluctuations shows significant scatter (Beresh *et. al.* 2010, figure 11). Figure 19 shows pressure r.m.s from the present simulations, normalized with $q_e = (1/2)\rho u_\infty^2$ and τ_{wall}, and plotted as a function of the streamwise distance x. In the turbulent region, $x > 6.5$, the normalized pressure fluctuations are fairly constant, and show a reasonable agreement with experimental results of Beresh *et. al.* (2010, figure 11). Note, however, that the peak pressure fluctuations are observed before the flow becomes fully turbulent, and the magnitudes are significantly larger than the fluctuations in the turbulent region of the flow.

Acknowledgments

This work was supported by NASA under the hypersonics NRA program under grant NNX08AB33A. Computer time for the simulations was provided by the Minnesota Supercomputing Institute (MSI).

References

[1]Baker, C. J. 1979 The laminar horseshoe vortex. *J. Fluid Mech.* **95:** 347–367.

[2]Bathel B. F., Danehy, P. M., Inman, J. A., Watkins, A. N., Jones, S. B., Lipford, W. E., Goodman, K. Z., Ivey, C. B. & Goyne, C. P. 2010 Hypersonic Laminar Boundary Layer Velocimetry with Discrete Roughness on a Flat Plate.

AIAAPaper 2010–4998.

[3]Beresh, S. J., Henfling, J. F., Spillers, R. W. & Pruette, O. M. 2010 Pressure Power Spectra Beneath a Supersonic Turbulent Boundary Layer. *AIAA Paper 2010*–4274.

[4]Casper, K.M., Beresh, S. J., Henfling, J. F., Spillers, R. W. & Schneider, S. P. 2009 Pressure Fluctuations in Laminar, Transitional, and Turbulent Hypersonic Boundary Layers. *AIAA Paper 2009*–4054.

[5]Danehy, P. M., Bathel, B., Ivey, C., Inman, J. A. & Jones, S. B. 2009 NO PLIF study of hypersonic transition over a discrete hemispherical roughness element. *AIAA Paper 2009*–394.

[6]Ergin, F. G. & White, E. B. 2006 Unsteady and Transitional Flows Behind Roughness Elements. *AIAA J.* **44** 11: 2504–2514.

[7]Iyer, P.S., Muppidi, S. & Mahesh, K. 2011 Roughness–induced transition in high speed flows. *AIAA Paper 2011*–566.

[8]Moin, P. & Mahesh, K. 1998 DIRECT NUMERICAL SIMULATION: A tool in turbulence research. *Annu. Rev. Fluid Mech.* **30 :** 539-578.

[9]Muppidi, S. & Mahesh, K. 2012 Direct numerical simulations of roughness–induced transition in supersonic boundary layers. *J. Fluid Mech.,* in press.

[10]Park, N. & Mahesh, K. 2007 Numerical and modeling issues in LES of compressible turbulent flows on unstructured grids. *AIAA Paper* 2007–722.

[11]Reda, D. C 2002 Review and Synthesis of Roughness-Dominated Transition Correlations for Reentry Applications. *J. Spacecraft and Rockets* **39** 2: 161–167.

[12]Reshotko, E. 2007 Is Re_θ/M_e a meaningful transition criterion ? *AIAA Paper 2007*–943.

[13]Schneider, S. P. 2008 Summary of Hypersonic Boundary-Layer Transition Experiments on Blunt Bodies with Roughness. *J. Spacecraft and Rockets* **45** 6: 1090–1105.